Article

Integrating Metal–Organic Frameworks and Polyamide 12 for Advanced Hydrogen Storage Through Powder Bed Fusion

Chengming Shang [1], Yaan Liu [1], Oana Ghita [1], Noa Lachman [2], Dong Wang [1,*] and Mi Tian [1,*]

[1] Department of Engineering, University of Exeter, Exeter EX4 4PY, UK;
[2] Department of Materials Science and Engineering, Tel Aviv University, Tel Aviv 6997801, Israel
* Correspondence: d.wang2@exeter.ac.uk (D.W.); m.tian@exeter.ac.uk (M.T.)

Abstract: This paper introduces a pioneering approach that combines ex situ synthesis with advanced manufacturing to develop ZIF-67-PA12 Nylon composites with mixed-matrix membranes (MMMs), with the goal of enhancing hydrogen storage systems. One method involves producing MOF-PA12 composite powders through an in situ process, which is then commonly used as a base powder for powder bed fusion (PBF) to fabricate various structures. However, developing the in situ MOF-PA12 matrix presents challenges, including limited spreadability and processability at higher MOF contents, as well as reduced porosity due to pore blockage by polymers, ultimately diminishing hydrogen storage capacity. To overcome these issues, PBF is employed to form PA12 powder into films, followed by the ex situ direct synthesis of ZIF-67 onto these substrates at loadings exceeding those typically used in conventional MMM composites. In this study, ZIF-67 mass loadings ranging from 2 to 30 wt.% were synthesized on both PA12 powder and printed film substrates, with loadings on printed PA12 films extended up to 60 wt.%. ZIF-67-PA12-60(f) demonstrated a hydrogen capacity of 0.56 wt.% and achieved 1.53 wt.% for ZIF-67-PA12-30(p); in comparison, PA12 exhibited a capacity of 0.38 wt.%. This was undertaken to explore a range of ZIF-67 Metal–organic frameworks (MOFs) to assess their impact on the properties of the composite, particularly for hydrogen storage applications. Our results demonstrate that ex situ-synthesized ZIF-67-PA12 composite MMMs, which can be used as a final product for direct application and do not require the use of in situ pre-synthesized powder for the PBF process, not only retain significant hydrogen storage capacities, but also offer advantages in terms of repeatability, cost-efficiency, and ease of production. These findings highlight the potential of this innovative composite material as a practical and efficient solution for hydrogen storage, paving the way for advancements in energy storage technologies.

Keywords: metal–organic framework; powder bed fusion; 3D printing; mixed-matrix membrane; hydrogen storage

1. Introduction

Hydrogen storage plays a critical role in the large-scale storage of renewable energy and the transition towards a low-carbon economy. As hydrogen gas can be produced from renewable sources, such as wind and solar energy, it presents a sustainable alternative to fossil fuels in the transportation and energy storage sectors. However, the primary obstacle lies in devising methods to store hydrogen in a safe, compact, and cost-effective manner [1–5]. The United States Department of Energy (DoE) has established benchmarks to steer research towards feasible hydrogen storage solutions. These benchmarks are instrumental in supporting the ambitious net-zero targets outlined in the UK Hydrogen Strategy, emphasizing the importance of evaluating systems comprehensively, including their operating conditions, lifecycle durability, and associated costs.

Conventionally, gas storage has been reliant on compression vessels, typically featuring a cylindrical body terminated with a hemispherical end to optimize pressure distribution. Type I vessels, which are predominantly metallic, have been the standard in industrial applications, offering limited capacity (20–30 MPa). Advancements in this area, such as the introduction of leak-resistant liners and composite materials for external wrapping, have culminated in Type IV vessels. These vessels showcase a remarkable storage density of 5.68 MJ L^{-1} at 70 MPa [6]. Despite these advancements, current systems fall short of meeting the DoE's requirements for light-duty vehicles, highlighting the need for innovative materials and technologies that could enhance the efficiency of compression vessels for hydrogen storage.

There are several low-cost materials with high theoretical hydrogen storage capacity, such as magnesium-based materials [7–10] and carbon-based materials [11–13]. However, the main challenge for practical onboard applications lies in balancing safety, storage efficiency, and economic viability. MOF–polymer composites, produced using 3D printing techniques, offer a safer and more efficient process for converting hydrogen into electricity in fuel cell vehicles. Metal–organic frameworks (MOFs), such as ZIF-67, have emerged as promising materials for solid-state hydrogen storage due to their high surface area, tunable pore size, and excellent thermal and chemical stability, which are critical for adsorbing large volumes of gases. Cobalt-based frameworks also provide unique catalytic properties, further enhancing their functionality for gas sorption [14–24]. MOFs can provide a high hydrogen storage capacity per unit volume and weight, and they can also release hydrogen via either a temperature or pressure swing process, making them suitable for a variety of gas storage applications [14,16–19,21,25–35]. However, MOFs are often synthesized as fine powders, which makes them difficult for industrial use. Fine powders are notoriously difficult to manage due to respiratory hazards during handling and their incompatibility with standard industrial equipment [36–38]. In recent years, there has been increasing interest in creating mixed-matrix membranes (MMMs) by incorporating MOF fillers into polymer matrices [35,36,38,39]. These MMMs harness the combined benefits of MOFs and polymers, leading to materials that exhibit high flexibility, good mechanical strength, long-term stability, and ease of processability; thus, they have been broadly applied throughout the fields of water treatment [40], gas separation [35,36], and gas storage [36]. Due to the poor adhesion at the interface between MOFs and polymers, challenges persist at high MOF filling loadings (>20 wt.%), with the presence of nonselective voids and filler agglomeration in MMMs [41]. To address this, it is critical to develop manufacturing routines that maintain the dense structure of the polymer without compromising its mechanical properties, while preserving the active porosities of MOFs to ensure excellent compatibility between MOFs and polymers.

Three-dimensional printing is an innovative fabrication method that enables the construction of three-dimensional objects through a layer-by-layer additive process, offering the advantages of fabricating intricate and customized geometries. Various techniques within 3D printing, such as Fused Deposition Modelling (FDM), Direct Ink Writing (DIW), and powder bed fusion (PBF), have been widely applied across different fields, including water treatment [39], gas storage [21], and energy storage [42]. Among these, PBF emerges as a highly effective technique for addressing the challenges associated with MOF–polymer composites [43–45]. This technique enables the construction of macro-porous structures with adjustable porosity, allowing for enhanced performance without compromising the ultra-micro-porosity and gas adsorption properties of MOFs [18,39]. This process provides a strategic approach to manipulate the physical properties of MOFs, facilitating their integration into practical applications of MOF–polymer membrane fabrication while maintaining the advantageous characteristics of MOFs for hydrogen storage and other gas storage applications [15,20,21,25].

Polyamide 12 (PA12) is a polymer widely used in additive manufacturing (AM) processes for its optimal combination of strength and flexibility, making it suitable for a wide range of applications, including the fabrication of MOF–polymer composites for gas

storage [18,46–48]. In particular, its chemical stability, good mechanical properties, and flexibility are vital for ensuring long-term durability in gas storage applications. Leveraging the unique properties of PA12 and building upon the existing literature related to in situ techniques for designing 2 wt.% ZIF-67-PA12 powder composites, referred to as ZIF-67@PA12, we aimed to fabricate hierarchical porous mixed-matrix membrane structures through the PBF process. However, a challenge arises with this technique when dealing with higher starting mass loadings, which affects the composite's efficiency due to spreadability and processability issues within the PBF [18]. To address this limitation, we introduce here a novel strategy that combines the PBF process with an ex situ MOF synthesis on a PA12 film membrane, where up to 60 wt.% initial mass loadings of ZIF-67 are grown on the surfaces of PBF-printed PA12 film. Additionally, this method helps reduce the high demand for pre-prepared ZIF-67-PA12 powder bed base powder. This ex situ strategy aims to enhance the hydrogen storage performance of the composites by preserving the active sites of ZIF-67 and ensuring their accessibility.

In this work, we explored two different strategies for fabricating ZIF-67-PA12 composites, as illustrated in Figure 1: (i) in situ synthesis combined with PBF, and (ii) a process that employs PBF followed by ex situ synthesis. The in situ approach involves the simultaneous synthesis of ZIF-67 with PA12 to form ZIF-67-PA12 powder. As the PBF process progresses, laser sintering fuses this composite powder to create the desired 3D structure. This method potentially offers a superior integration of ZIF-67 into the polymer matrix, enhancing the structural integrity due to the homogeneous distribution of ZIF-67 particles. In contrast, our new strategy involves first creating 3D-printed membranes using pure PA12. Post-printing, this structure is then subjected to an ex situ synthesis process where it is infused with ZIF-67 precursors in a subsequent step. This secondary process involves soaking the 3D-printed polyamide in a solution containing MOF precursors, followed by an isothermal synthesis to coat ZIF-67 onto the PA12 films. This method might be preferable for achieving higher MOF loadings, saving the excessive production of MOFs.
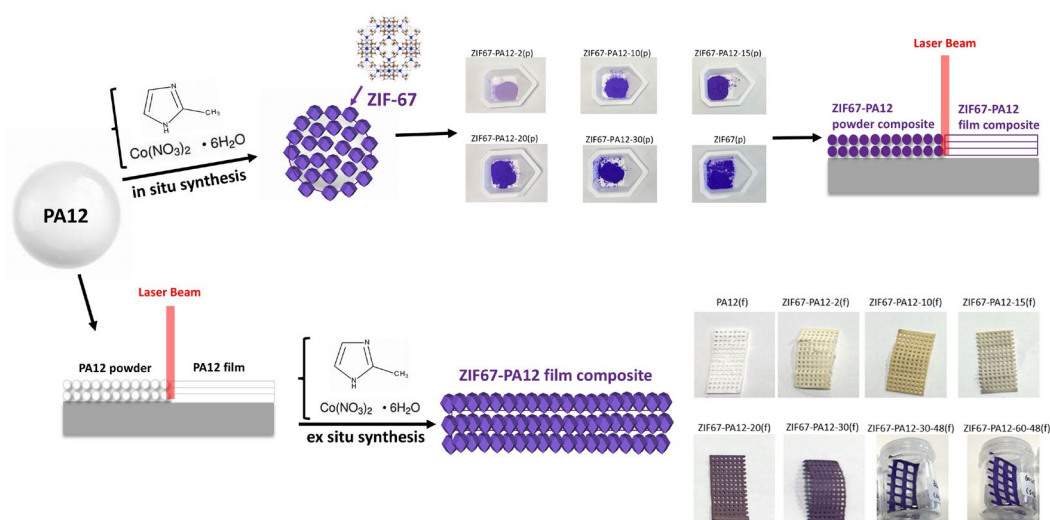
Figure 1. Schematic procedure for in situ synthesis of ZIF-67@ PA12 composite powder and ex situ synthesis of ZIF-67@PA12 film using PBF.

This work focused on the ex situ method, exploring the effects of different mass loadings of starting materials and synthesis duration on particle size, the dispersion of ZIF-67, and the hydrogen storage properties of the ZIF-67@PA12 composite. Structural, morphological, surface, thermal, and gas analysis were studied to reveal the structural properties

of the materials and to establish a correlation between their structural characteristics and their capacity for hydrogen storage. Our findings demonstrated that our innovative ex situ approach successfully integrates ZIF-67 onto the surface of 3D-printed PA12 membranes, effectively preserving the MOF's porous structure, which is essential for efficient gas adsorption. Importantly, we identified a significant relationship between the concentration of ZIF-67 within the ZIF-67@PA12 composites and their hydrogen storage performance. These results not only underscore the potential of MOF–polymer composites in enhancing gas storage solutions, but also represent a significant breakthrough in the additive manufacturing domain. Such innovations in ex situ-synthesized composites with high MOF starting mass loadings of 60 wt.% and the potential for higher MOF actual content are poised to significantly impact hydrogen storage and other related fields, including onboard hydrogen storage systems, paving the way for further research into the 3D printing of MOF–polymer composites and their application in advanced energy storage solutions.

2. Methods and Experiments

2.1. Materials

Polyamide 12, PA12, or Nylon12 (PA12, PA2200), was purchased from EOS (Gmbh, Krailling, Germany); cobalt nitrate hexahydrate ($CO(NO_3)_2 \cdot 6H_2O$) and 2-Methylimidazole (MIM) were purchased from Sigma-Aldrich (St. Louis, MO, USA).

2.2. In Situ and Ex Situ Synthesis of MOFs

The in-situ synthesis of ZIF-67-PA12 powder samples was undertaken. The method for synthesizing ZIF-67 was based on a previous study [18,39]. For the synthesis of ZIF-67-PA12 powder composites, the procedure involved separately dissolving a portion of cobalt nitrate hexahydrate ($CO(NO_3)_2 \cdot 6H_2O$) in proportioned distilled water and adding PA12 powder (PA2200) of a fixed ratio to a solution containing fully dissolved and proportioned 2-Methylimidazole (MIM) in deionized water. The two solutions were mixed under vigorous stirring at 60 °C. Synthesis yield was used to calculate the amount of final product recovered after all the synthesis and purification steps were completed (Table S1). The weight percentages of ZIF-67 to PA12 used for synthesis were 2, 10, 15, 20, and 30, corresponding to ZIF-67-PA12-2(P), ZIF-67-PA12-10(P), ZIF-67-PA12-15(P), ZIF-67-PA12-20(P), and ZIF-67-PA12-30(P), respectively.

The fabrication of PA12 films involved using a CO_2 laser with a Sharebot Snowwhite system. The parameters for the process were started with a laser power of 4.2 W, a laser speed of 2400 mm/s, and a layer thickness of 0.1 mm. The operating temperature was set at 185 °C with 20 warming layers. The calculated energy density was 0.018 J/mm².

The ex-situ synthesis of ZIF-67-PA12 film samples was undertaken. Subsequent to laser sintering, these PA12 films underwent ex situ synthesis by being immersed in a ZIF-67 precursor solution under various conditions for ZIF-67 formation and incorporation. The synthesis of ZIF-67 mass loadings of 2, 10, 15, 20, and 30% involved a similar synthesis condition to the composite powders, with varying amounts of distilled water, cobalt nitrate hexahydrate, 2-methylimidazole, and PA12 based on the respective weight percentages (Table S2). The resulting composites were labelled as ZIF-67-PA12-2(f), ZIF-67-PA12-10(f), ZIF-67-PA12-15(f), ZIF-67-PA12-20(f), and ZIF-67-PA12-30(f). To study the effects of reaction time, the composite with 30 wt.% ZIF-67 was stirred in solvent for 48 h, resulting in a product labelled as ZIF-67-PA12-30-48(f).

The actual concentrations of ZIF-67 in the various ZIF-67-PA12 powder composites were determined from the residual percentages of cobalt measured at 750 °C obtained from thermal gravimetric analysis (TGA) data. For the calculation, see Equation (1).

$$\text{Actual concentrations of ZIF67} = \frac{R_{Cobalt}\text{wt. \% in ZIF67@PA12 composites}}{R_{Cobalt}\text{wt. \% in ZIF67}} \tag{1}$$

In Equation (1), the calculation of the actual concentrations of ZIF-67 in the ZIF-67-PA12 composites with cobalt is undertaken, with residual percentages measured at 750 °C. *R* stands for material residual content.

2.3. Material Characterisation

XRD patterns were recorded on a Bruker D8 advanced X-ray diffractometer with Cu Kα radiation (40 kV-40 mA) at a step time of 1 s and a step size of 0.02°.

Field-emission SEM images were recorded using a Nova Nanolab 600 scanning electron microscope (Thermo Fisher Scientific, Hillsboro, Oregon, USA) with the electron beam in high-vacuum mode and a voltage of 10 kV. All samples were coated with a 20 nm thick Cr layer beforehand. EDS data were acquired from an xT Nova Nanolab 600 FIB at 15 kV to determine the elemental composition of the sample.

The TGA data were obtained using TGA55 equipment (TA Instruments, New Castle, DE, USA) and ~15 mg samples, which were heated from room temperature (25 °C) up to 800 °C at 10 °C min^{-1} under a nitrogen atmosphere.

Nitrogen adsorption/desorption isotherms were measured by a Quantachrome Autosorb-iQ gas sorptometer (Quantachrome Instruments, Anton Paar—Autosorb-iQ

model, Miami, FL, USA) and calculated via the Brunauer–Emmett–Teller (BET) method based on adsorption data in the partial pressure (P/Po) range of 0.05–0.20. The pore size distribution (PSD) was measured by analysing the adsorption and desorption isotherms using the Density Functional Theory (DFT) model. Micrographs were photographed under a Keyence VHX-7000 light microscope(Keyence Corporation, Osaka, Japan).

2.4. Hydrogen Adsorption and Desorption Measurements

H$_2$ gas adsorption capacities were investigated on an IGA-003 (Hiden Isochema, Warrington, UK) instrument using ~50 mg for powder samples and ~70 mg for film samples. Prior to the gas adsorption analysis, the samples were purged with helium gas and skeletal density was measured at room temperature with helium gas. Then, the samples were dried under a vacuum state at 120 °C for 8 h and the H_2 excess adsorption measurements were carried out at −196 °C (77 K) from 0 to 20 bars at a flow rate of 200 Mbar/minute using CP-grade hydrogen.

3. Results and Discussion

3.1. Morphology Analysis

Synthesized ZIF-67 powder, as previously reported [18], presents in a dark-violet color (Figure 1). For the ZIF-67-PA12 powder composites, the color progressively transitions into a darkened violet shade with increasing loadings of ZIF-67. Similarly, for film composites, there is a clear and discernible color transition from white to purple. These observations primarily corroborate the successful formation of ZIF-67 onto the PA12 particle surface and the printed PA12 films, as illustrated in Figure 1.

The crystalline structures of ZIF-67-PA12 powder and film composites were characterized by powder X-ray diffraction (XRD), as shown in Figure 2a and 2b, respectively. The XRD patterns for both the powder and film composites, especially those with higher ZIF-67 mass loadings, exhibit distinct peaks that algin with the known diffraction patterns of both ZIF-67 and PA12 [18]. The presence of characteristic peaks specific to ZIF-67 indicates that the metal–organic framework has been successfully synthesized and incorporated within the composite. Furthermore, the retention of PA12 peaks suggests that the polymer's crystallinity remains unaffected by the process of embedding ZIF-67, which is crucial for maintaining the material's mechanical properties. c displays the ex situ-synthesized freestanding ZIF-67-PA12 composite film. The cross-sectional micrograph of printed PA12 film reveals an uneven surface with observed voids, serving as open sites for ZIF-67 to root within the gaps during ex situ synthesis (Figure S1). Figure 2d shows a cross-

sectional micrograph of a ZIF-67-PA12 film composite, revealing the growing pattern of ZIF-67 clusters on the surface of the PA12 film. This setup reveals the unique characteristics of PBF, allowing the landing and growing of ZIF-67 on PA12 films in ex situ synthesis processes, and demonstrates the uniform distribution of ZIF-67 on PA12 matrix surfaces. Importantly, this configuration is crucial for maintaining the inherent porosity of ZIF-67, which is essential for its effectiveness in gas adsorption applications.
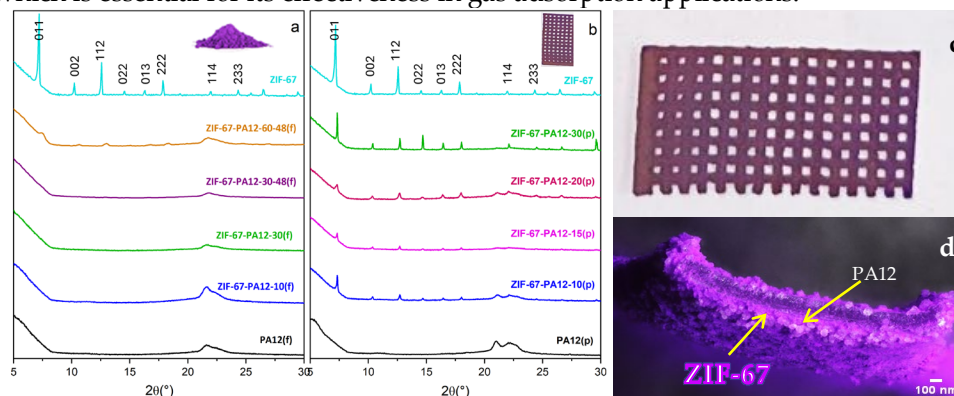
Figure 2. (**a**) XRD patterns of ZIF-67-PA12 powder composites; (**b**) XRD patterns of ZIF-67-PA12 film composites; (**c**) a photo of ZIF-67-PA12 composite film and (**d**) its cross-sectional micrograph.

SEM offers detailed morphology of the prepared samples. As the SEM images illustrate, the successfully formed ZIF-67 manifests in a rhombic shape with a mean particle size distribution of 1.75 μm (Figure 3a). Both PA12 power and 3D-printed film have a rough surface, which positively affects the growth of ZIF-67 (Figure 3b,c), influencing crystal nucleation and attachment. Notably, even at a low ZIF-67 concentration of 2 wt.%, ZIF-67 crystals still can be observed on the surface of PA12 particles (Figure 3d), indicating that the initial stage of MOF formation is facilitated by substrate roughness [49]. For powder composites, increasing mass loadings observed via SEM confirm the successful formation of ZIF-67 crystals across the PA12 surface, with particle size progressively increasing. From ZIF-67-PA12-2 to ZIF-67-PA12-20, the average particle size ranges between 0.36 and 0.56 μm. When the ZIF-67 content further increases in ZIF-67-PA12-30, the crystals expand to a mean size of 0.97 μm, approaching the rhombic shape typical of fully synthesized ZIF-67, and incrementally cover the entire surface of the PA12 particles with good dispersion (Figure 3d–h). This suggests that higher concentrations of ZIF-67 lead to more extensive surface coverage, enhancing the potential for improved gas adsorption properties due to increased MOF presence.

For film composites, extended synthesis durations result in larger particles. From ZIF-67-PA12-30-24 to ZIF-67-PA12-30-48, both samples maintain an initial MOF mass loading of 30 wt.%, but when the synthesis duration is doubled from 24 to 48 h, the mean particle size increases from 0.75 μm to 1.72 μm, approaching the 0.97 μm size of fully synthesized ZIF-67. Additionally, beyond synthesis time, the initial mass loading of ZIF-67 significantly influences particle size. SEM and particle size distribution data show more clustered ZIF-67 formations, with a clear increase in mean particle size reaching 1.98 μm (Figure 3i–o). This observation is crucial as it indicates that synthesis time and starting MOF loading are key variables affecting the morphology and possibly the functional properties of the composite films. Longer durations facilitate the growth of larger ZIF-67 clusters, which will impact the diffusion and accessibility of adsorbate molecules, thereby affecting the overall efficiency of gas adsorption. The film composites of ZIF-67-PA12 were also analyzed using energy-dispersive X-ray spectroscopy (EDS), as shown in Figure S2. The findings verified that as the initial mass loading increased, the dispersion of ZIF-67 crystals improved and became more widespread.
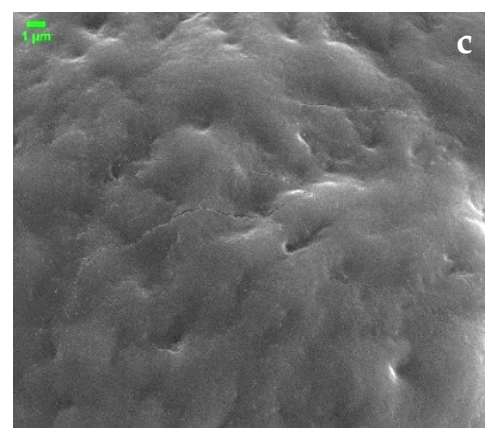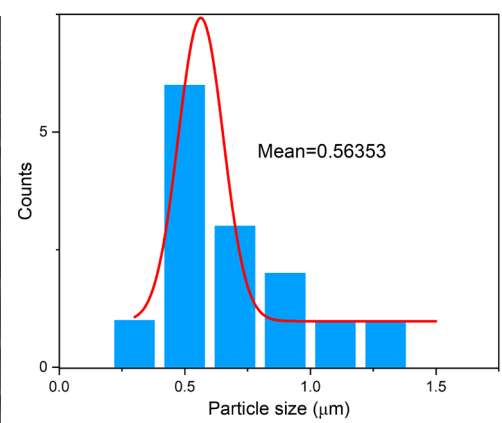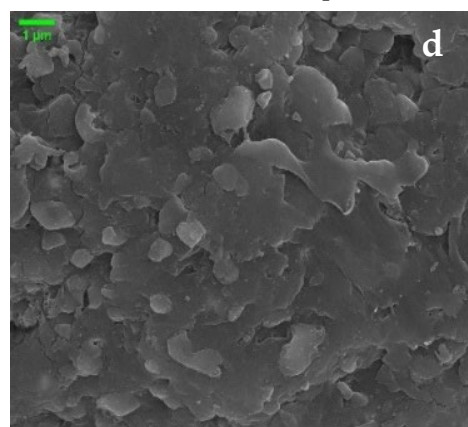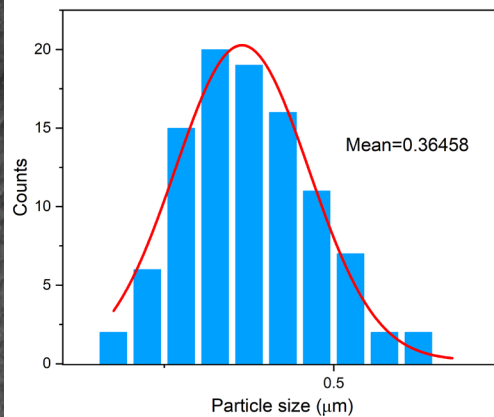
ZIF-67(p)
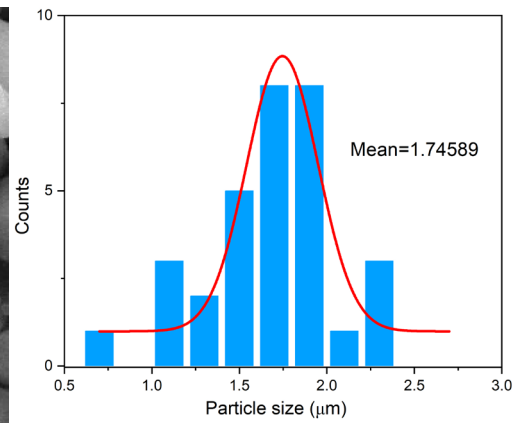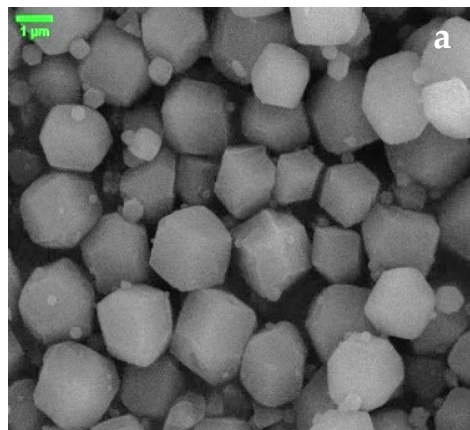
PA12(p)
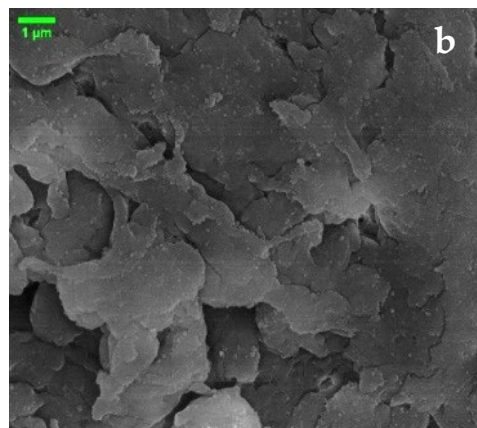
PA12(f)

ZIF-67-PA12-2(p)
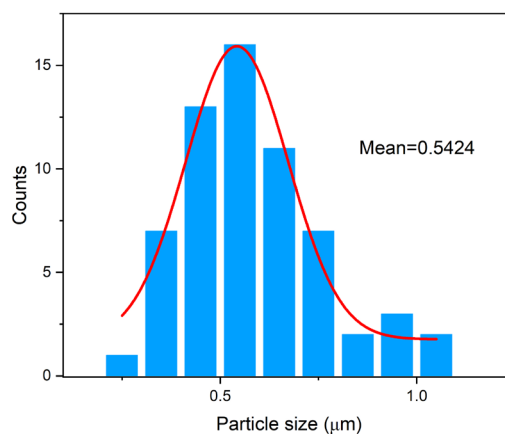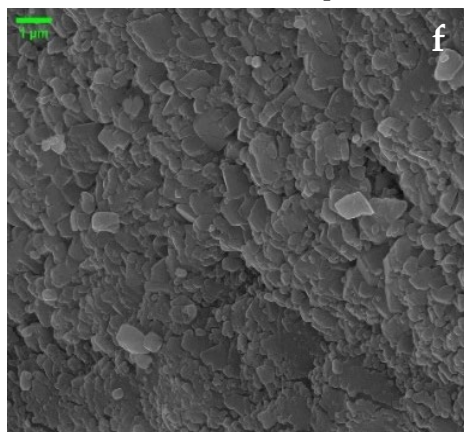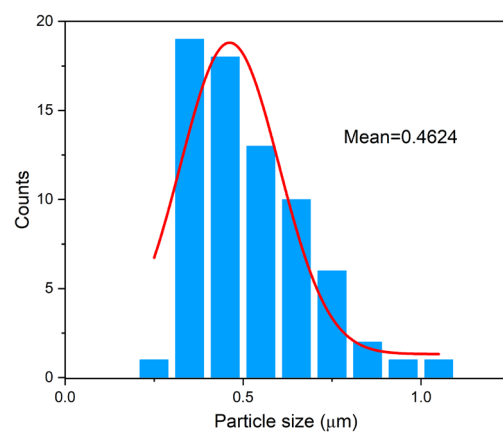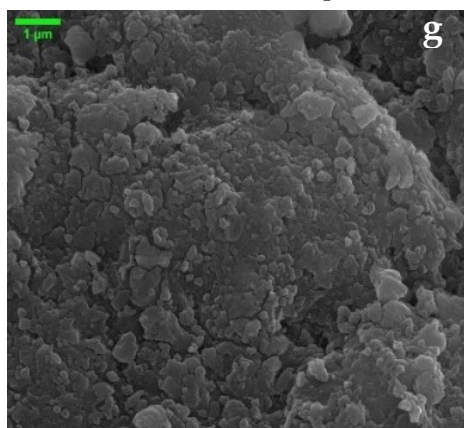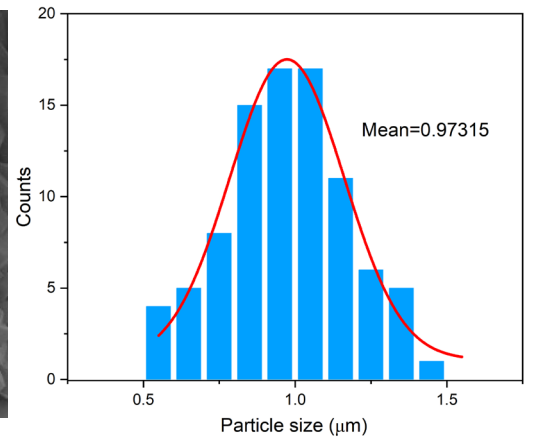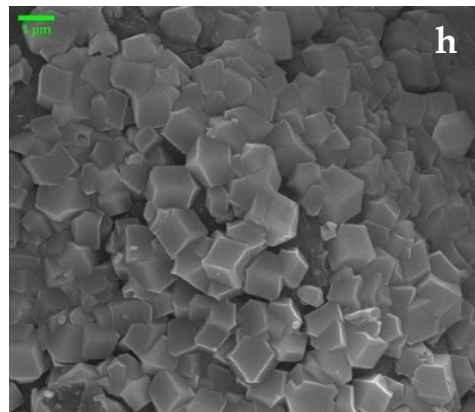
ZIF-67-PA12-10(p)
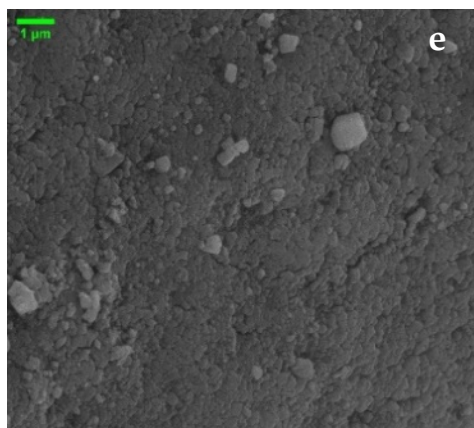
ZIF-67-PA12-15(p)

ZIF-67-PA12-20(p)

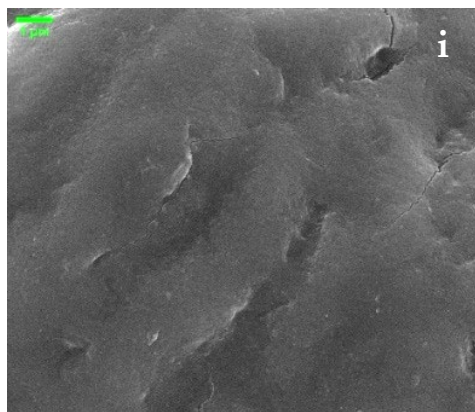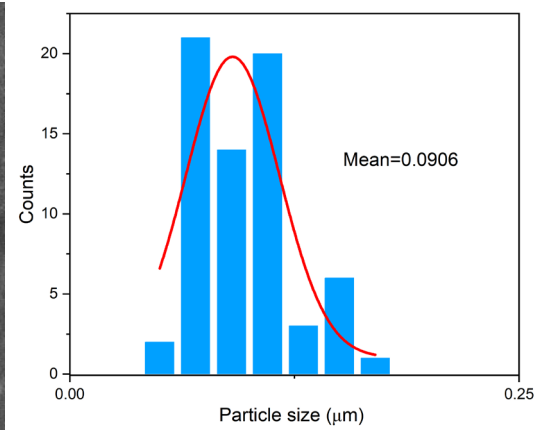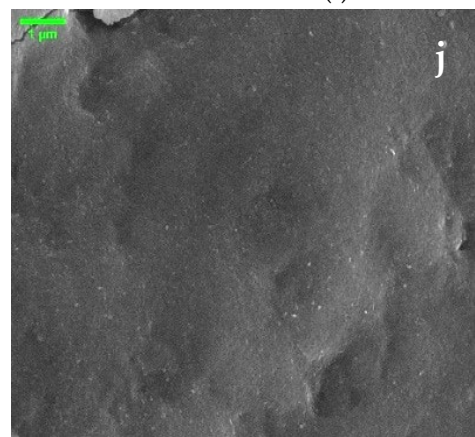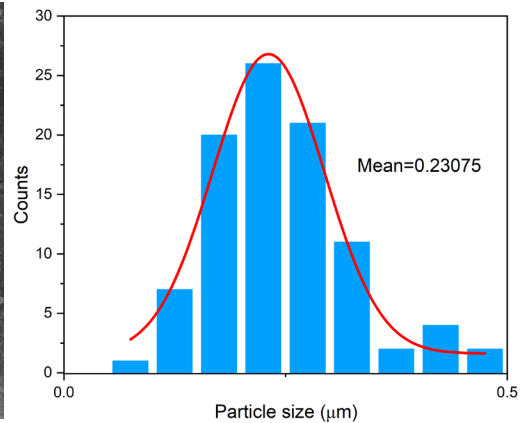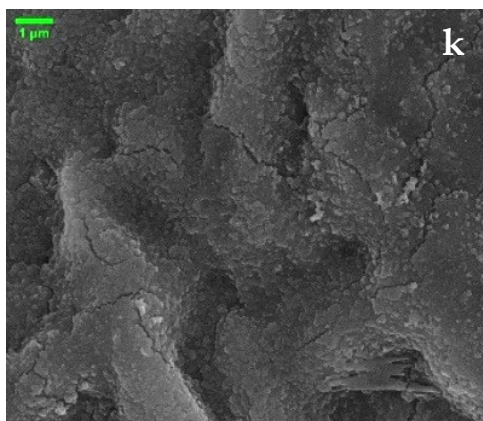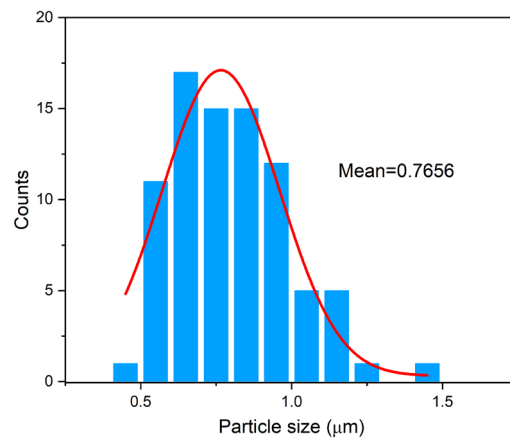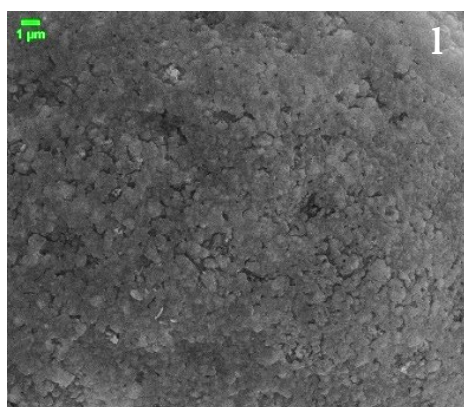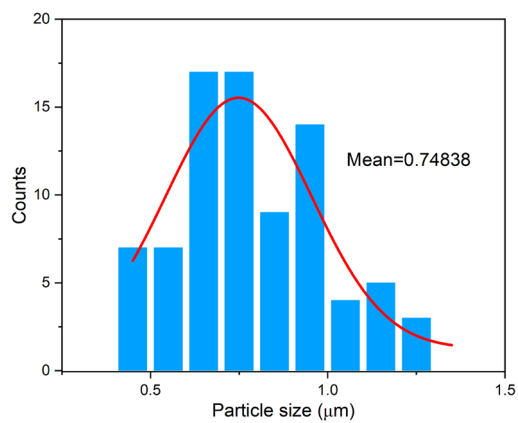ZIF-67-PA12-30(p)

ZIF-67-PA12-2(f)

ZIF-67-PA12-10(f)
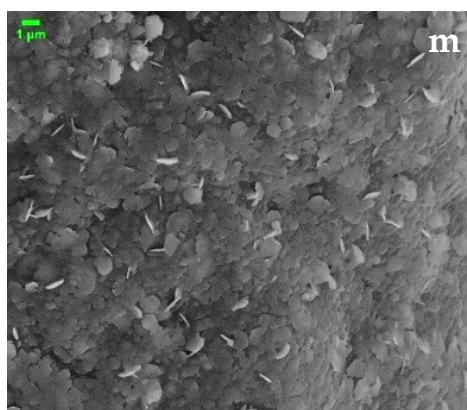
ZIF-67-PA12-15(f)

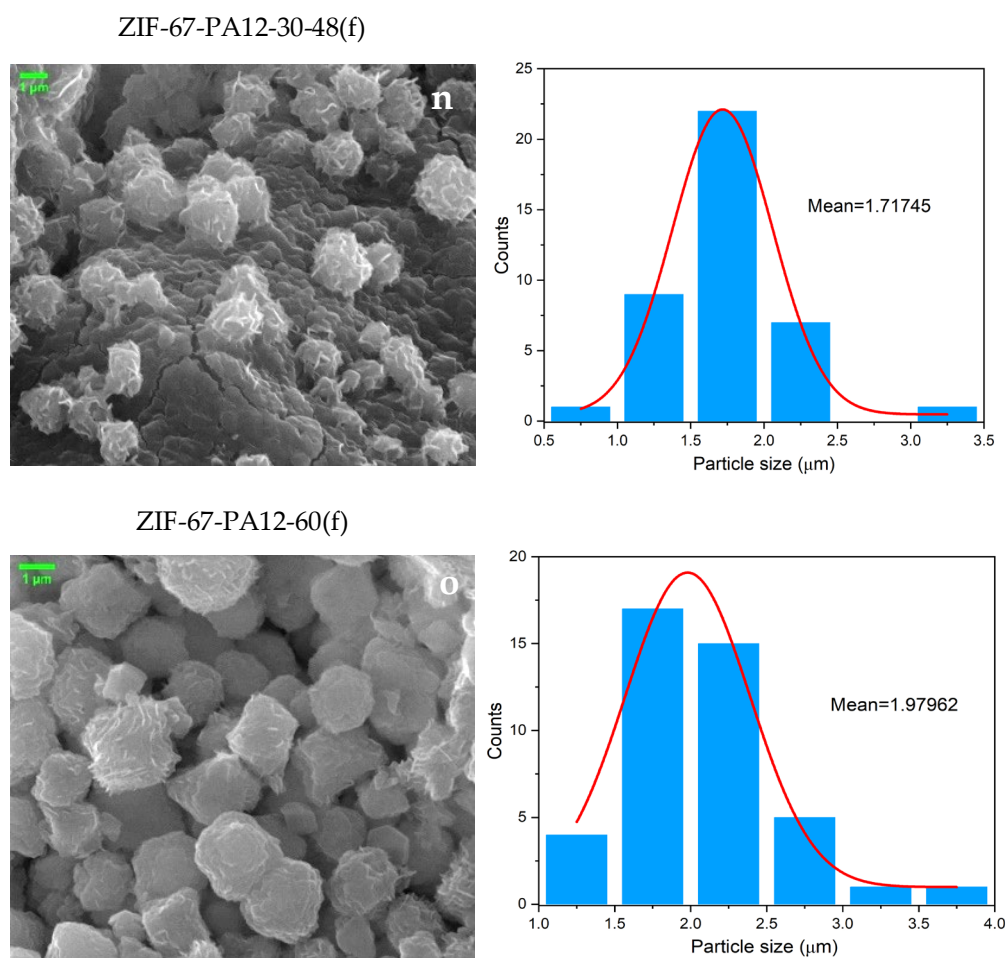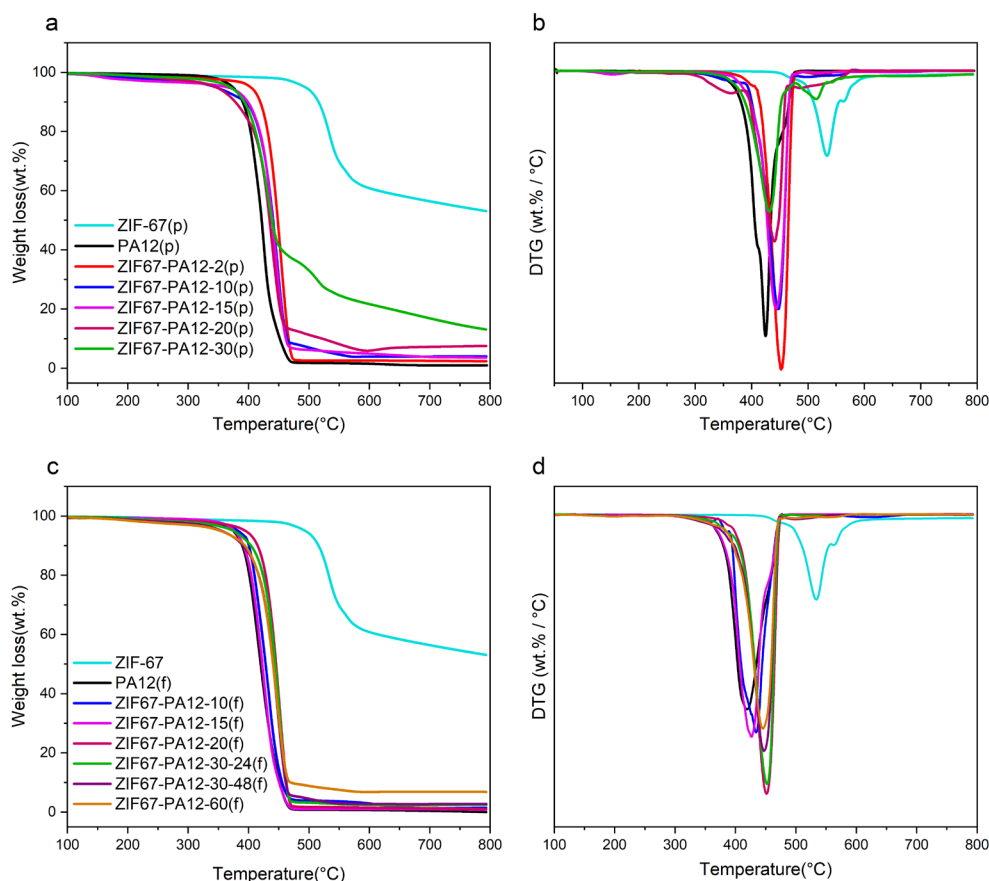ZIF-67-PA12-20(f)

ZIF-67-PA12-30-24(f)

ZIF-67-PA12-30-48(f)

ZIF-67-PA12-60(f)

Figure 3. (**a–g**) SEM images and corresponding particle size distribution charts with red curve representing the cumulative distribution of particle sizes for PA12 powder, ZIF-67, ZIF-67-PA12-2, 10, 15, and 20(p) powder composites. (**h–o**) SEM images and corresponding particle size distribution charts with red curve representing the cumulative distribution of particle sizes for PA12 film, ZIF-67-PA12-2, 10, 15, 20, 30-24, 30-48, and 60 (**f**) film composites.

3.2. Thermogravimetric Analysis and BET Surface Area

Thermogravimetric analysis (TGA) was employed to evaluate the thermal stability of the samples and quantify the actual content of ZIF-67 within ZIF-67-PA12 composite powders (Figure 4a). The differential thermogravimetry analysis (DTG) curves represent the temperatures at which the material's weight is decreasing most rapidly, which corresponds to significant thermal degradation or decomposition (Figure 4b), demonstrating that all ZIF-67-PA12 composite powders are thermally stable up to 300 °C in a N_2 atmosphere. With the increasing loading contents of ZIF-67 in powder composites, the onset and peak temperatures shift to the higher temperature characteristic of ZIF-67. For the ZIF-67-PA12-30 powder, two distinct degradation peaks are observed: the first at 429 °C aligns with PA12, while the subsequent peak at 516 °C corresponds with the thermal degradation temperature of ZIF-67 powder, indicating the successful in situ synthesis of ZIF-67-PA12 powder. The clear differentiation of thermal degradation points between the polymer and the MOF component (ZIF-67) in the composite indicates that the ZIF-67 has been effectively synthesized within the PA12 matrix without altering its intrinsic thermal degradation properties. This successful in situ synthesis not only ensures the integrity and dispersion of ZIF-67 within the composite, but also enhances the composite's utility by combining the properties of both components effectively.

For film composites, the thermal behavior contrasts with that of the powder composites in Figure 4c,d. The DTG highlights a single degradation peak for each of the film composites, where the thermal degradation temperature increases from 415 °C for plain PA12 film to 450 °C for ZIF-67-PA12-20, 30, and 60. This suggests a greatly improved thermal stability of ZIF-67-PA12 film composites and superior interfacial linking between ZIF-67 and PA12 films compared to the composite powder (Figure 4d).

This enhanced thermal stability with increasing ZIF-67 content, ensuring that the MOF retains its crystal structure at elevated degradation temperatures, is essential in consideration of practical onboard hydrogen storage. Composites with improved thermal stability can better withstand the thermal fluctuations typically experienced during vehicle operation, thereby preventing the collapse or deformation of their crystal and porous structures, and ensuring reliable performance during gas adsorption–desorption cycling.

Figure 4. (**a**) TGA curves of ZIF-67, PA12, and ZIF-67-PA12 powders. (**b**) DTG curves of ZIF-67, plain PA12, and ZIF-67-PA12 powders. (**c**) TGA curves of PA12 and ZIF-67-PA12 films. (**d**) DTG of PA12 and ZIF-67-PA12 film in a nitrogen atmosphere at a heating rate of 10 °C/min.

Plain PA12 powder has a melting temperature around 180 °C [48]. By calculating the actual contents of ZIF-67 in these composites, the results reveal that the actual contents of ZIF-67 in the powder composites are very close to their theoretical concentrations; for example, ZIF-67-PA12-30(p) has a 30% initial concentration and a 28% actual concentration (shown in Table 1). However, for the composite films, the actual concentrations are significantly lower; for instance, ZIF-67-PA12-30-48(f), with 30% initial ZIF-67 loading for a 48h reaction time, achieved an actual concentration of 5 wt.%, and the highest actual concentration was 13 wt.% for a 60 wt.% initial ZIF-67 loading. PA12 powder exhibits a high surface-area-to-volume ratio, but when printed parts sinter powder particles together, the resulting reduction in surface area limits the available sites for MOF growth, leading to lower actual concentrations of ZIF-67. However, with the similar actual ZIF-67 content of

13–14 wt.%, ZIF-67-PA12-60(f) is found to be 12 °C higher than ZIF-67-PA12-20(p) in the data collected for thermal degradation, suggesting that synthesized film composites are more thermally stable than synthesized powder composites. This could be the result of better interfacial linking with different growing patterns in film and powder composites. ZIF-67 can form a consecutive coating of ZIF-67 on existing ZIF-67 layers during the synthesis of film composites and eventually form the morphology of ZIF-67 clusters (see Figure 3o), as also mentioned in [18], maximizing the contact area. This extensive contact enhances the chances of ZIF-67 to grow on both polymers, andZIF-67 itself as a growing substrate.

Table 1. Theoretical and actual ZIF-67 contents in various composites, as calculated from TGA results for ZIF-67, PA12, and ZIF-67-PA12 powders and ZIF-67-PA12 films.

Sample	Theoretical Contents of ZIF-67 (wt.%)	Actual Contents of ZIF-67 (wt.%)	Thermal Degradation Temperature (℃)
ZIF-67	-	-	535
PA12 powder	-	-	425
ZIF-67-PA12-2(p)	2	5	452
ZIF-67-PA12-10(p)	10	8	448
ZIF-67-PA12-15(p)	15	8	445
ZIF-67-PA12-20(p)	20	14	438
ZIF-67-PA12-30(p)	30	28	429/516
ZIF-67-PA12-10(f)	10	3	435
ZIF-67-PA12-15(f)	15	3	425
ZIF-67-PA12-20(f)	20	2	450
ZIF-67-PA12-30-24(f)	30	5	450
ZIF-67-PA12-30-48(f)	30	5	450
ZIF-67-PA12-60(f)	60	13	450

Nitrogen isotherms were used to calculate the BET surface area and porosity of all samples. The N_2 isotherms are Type I isotherms, indicating microporosity (Figure 5a,b). The N_2 adsorption increases with the rising content of ZIF-67 in the composites, demonstrating the enhanced porosity attributed to the incorporation of ZIF-67. The BET surface area exhibits a notable increase in both the powder and film composites with the rise in actual ZIF-67 content from 89 m^2/g for PA12 powder, 785 m^2/g for ZIF-67-PA12-30(p), and 135 m^2/g for ZIF-67-PA12-60(f). ZIF-67 is a highly porous material with a BET surface area of 1243 m^2/g (Table 2). These data clearly demonstrate that the BET surface area increases proportionately with an enhanced actual content of ZIF-67, reflecting the significant impact of ZIF-67 integration on the composites' adsorptive properties.

Figure 5b shows the PSD of ZIF-67 with a narrow pore size centered at 1 nm and a small proportion of mesopores, typical of ZIF-67. The pore size of PA12 is larger than 2 nm, as shown in Figure 5b. The PSD of the synthesized ZIF-67-PA12 powder composites, with the exception of ZIF-67-PA12-2, predominantly aligns with the characteristic range of both ZIF-67 and PA12. This suggests a successful integration of ZIF-67's microporous properties with the PA12 matrix, potentially leading to a hybrid material that combines the high surface area and microporosity of ZIF-67 with the processibility of PA12. Among all synthesized ZIF-67-PA12 film composites, ZIF-67-PA12-60(f) has the highest actual ZIF content, having a PSD pattern aligned with ZIF-67 and PA12 (Figure 5c and d).
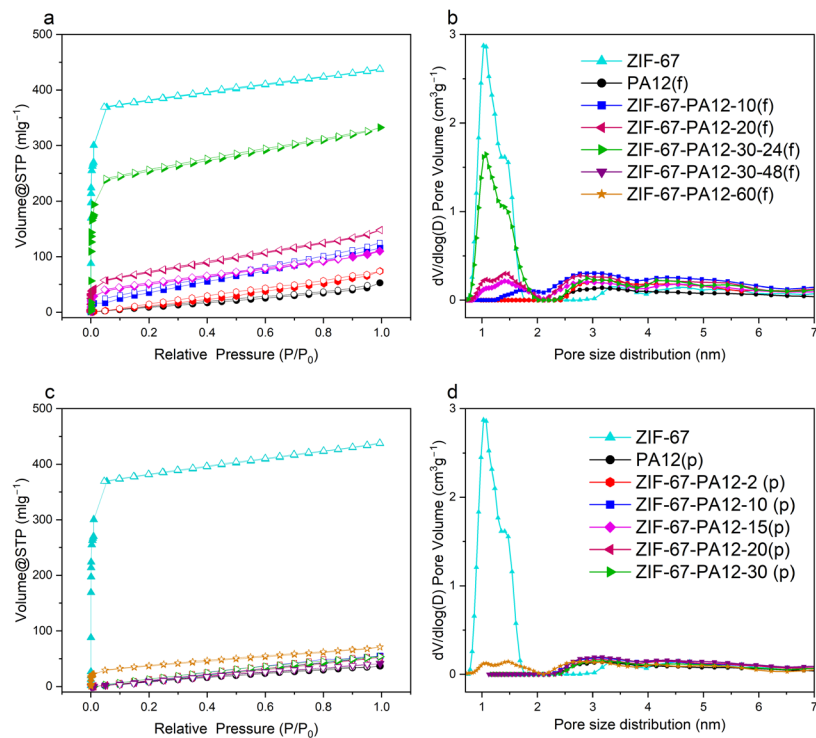
Figure 5. (**a**) Nitrogen isotherms for ZIF-67, PA12 powders, and ZIF-67-PA12 composite powder (**b**) Nitrogen sorption isotherms for ZIF-67, PA12 film, and ZIF-67-PA12 films. Each sample is assigned a unique color and a corresponding symbol for the collected data points, full symbol for nitrogen adsorption, empty symbol for desorption. (**c**) Pore size distribution of ZIF-67, PA12, and ZIF-67-PA12 composite powders. (**d**) Pore size distribution of ZIF-67, PA12 film, and ZIF-67-PA12 composite films.

Table 2. Calculated BET surface areas of ZIF-67, PA12, ZIF-67-PA12 powders, and ZIF-67-PA12 films.

Sample	Specific Surface Area (m^2/g)
ZIF-67	1243
PA12 powder	89
ZIF-67-PA12-2(p)	156
ZIF-67-PA12-10(p)	163
ZIF-67-PA12-15(p)	187
ZIF-67-PA12-20(p)	260
ZIF-67-PA12-30(p)	785
ZIF-67-PA12-10(f)	117
ZIF-67-PA12-15(f)	-
ZIF-67-PA12-20(f)	138
ZIF-67-PA12-30-24(f)	176
ZIF-67-PA12-30-48(f)	168
ZIF-67-PA12-60(f)	135

3.3. Hydrogen Storage and Kinetics

The H_2 sorption isotherms were obtained at 77 K up to 20 bars, as shown in Figure 6. Compared to the negligible hydrogen storage capacity of plain PA12, both the ZIF-67-PA12 composite powders and films exhibited a remarkable enhancement in H_2 storage

capacity. Specifically, ZIF-67-PA12-60(f) demonstrated a hydrogen capacity of 0.56 wt.% and achieved 1.53 wt.% for ZIF-67-PA12-30(p), while PA12 exhibited a capacity of 0.38 wt.%. This significant enhancement in hydrogen storage capacity highlights the effectiveness of incorporating ZIF-67 into the polymer matrix. Figure 7 shows three consecutive cycles of hydrogen sorption on ZIF-67-PA12-60(f), indicating an initial decline in hydrogen capacity that stabilized in subsequent cycles. The initial decline in hydrogen capacity suggests some degradation or structural rearrangement of the composite material that may occur during the first adsorption–desorption cycle. However, the stabilization of capacity in subsequent cycles indicates that the material reaches a steady state of performance, which is promising for repeated use. The hydrogen sorption across all samples was found to be completely reversible.
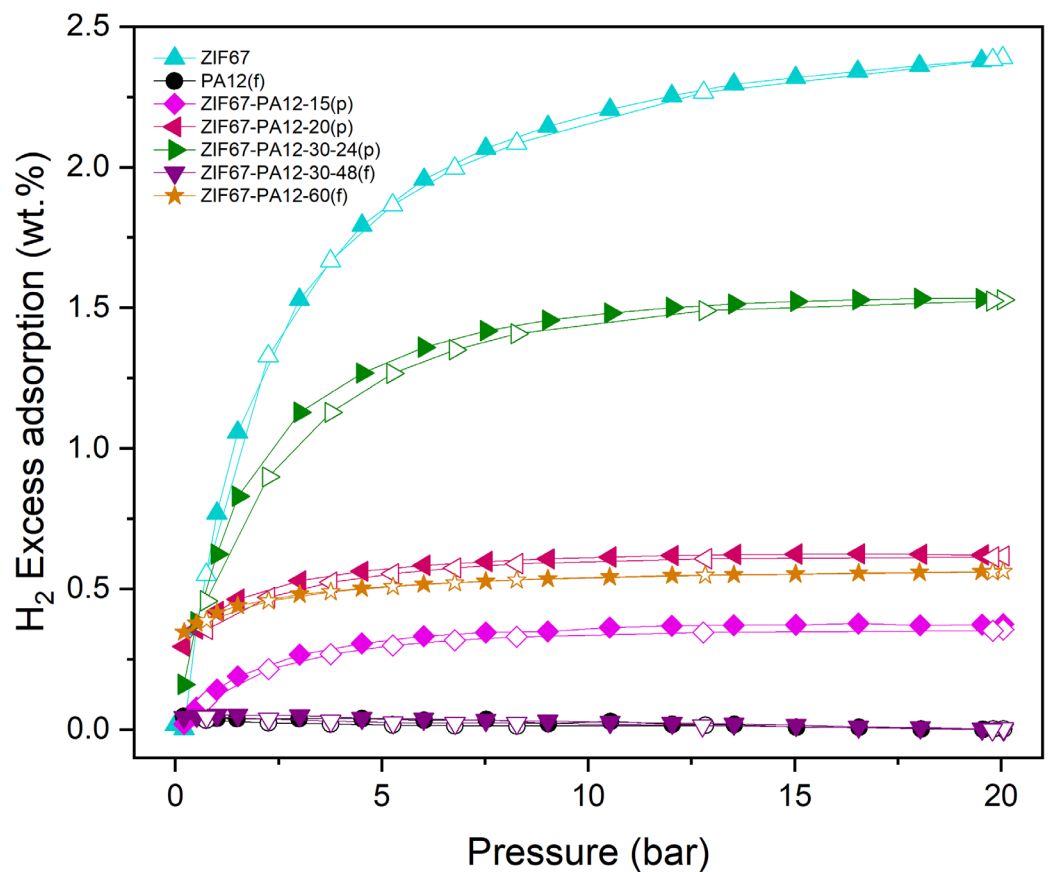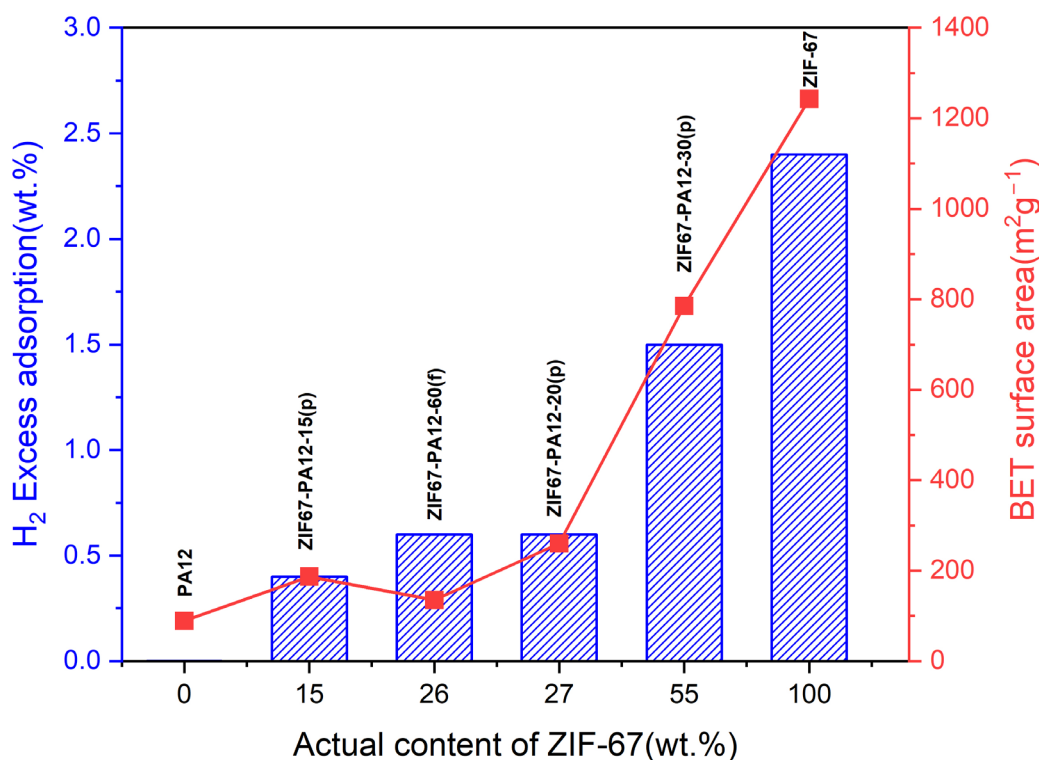

Figure 6. Hydrogen storage capacity of ZIF-67, PA12, and ZIF-67-PA12 powders and films at 77 K and 20 bar (shown for comparison). Each sample is assigned a unique color and a corresponding symbol for the collected data points, full symbol for nitrogen adsorption, empty symbol for desorption.
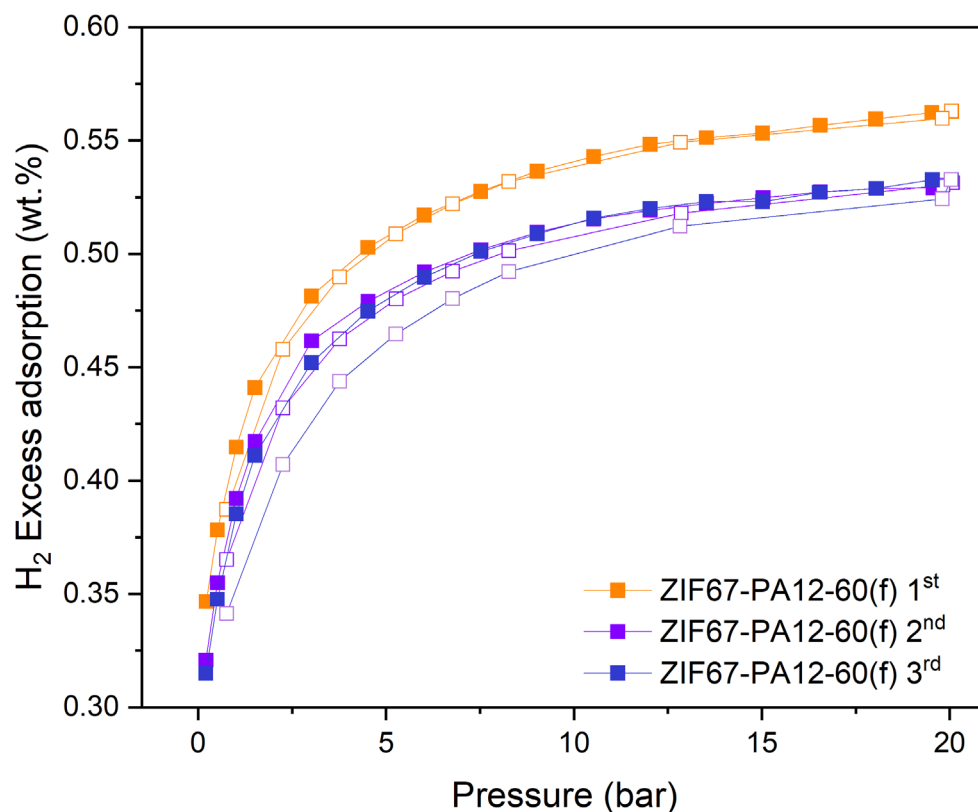
Figure 7. Hydrogen sorption isotherm of ZIF-67-PA12-60(f) with three consecutive cycles. Each sample is assigned a unique color and a corresponding symbol for the collected data points, full symbol for nitrogen adsorption, empty symbol for desorption.

To establish the relationship between the actual content of ZIF-67 and performance, Figure 8 plots both BET surface area and hydrogen storage capacity as functions of ZIF-67 concentration. The surface area directly correlates with hydrogen storage capacity, indicating that the increased surface area provided by higher ZIF-67 content significantly enhances the material's ability to adsorb hydrogen. This strong correlation demonstrates that the porosity introduced by ZIF-67 is vital for hydrogen adsorption, with higher porosity allowing more hydrogen molecules to adsorb onto the material's surface. Variations in the performance of ZIF-67-PA12 composites, such as those observed for ZIF-67-PA12-60(f), could stem from differences in composite processing or the distribution of ZIF-67 within the matrix. These minor discrepancies underscore the sensitivity of hydrogen storage performance to the physical characteristics of the composite.

Figure 8. Hydrogen storage capacity and BET surface area as a function of actual content of ZIF-67 in the ZIF-67-PA12 composites.

Hydrogen adsorption kinetic rate, K, is calculated using the Linear Driving Force (LDF) model [50] to analyze the rate of hydrogen gas diffusion in the materials. For each H_2 adsorption isotherm, the LDF model was applied to determine the kinetic rate corresponding to each dosing step. The LDF model assumes that the rate of adsorption is proportional to the difference between the current amount absorbed and the equilibrium amount (Equation (2)). A higher k value indicates a faster adsorption rate, while b represents the equilibrium amount of hydrogen that can be adsorbed. For practical implications, a faster kinetic rate is directly proportional to the speed at which hydrogen can be absorbed by the storage medium, resulting in predictable performance during the refueling of hydrogen-powered vehicles. A higher K value facilitates a quicker adsorption of hydrogen into storage tanks, enhancing the overall efficiency of the refueling process. The model's quality was confirmed by an adjusted R^2 value of ≥0.97, indicating high-quality fitting (Figure 9). Notably, the rates of ZIF-67, ZIF-67-PA12-30(p), and ZIF-67-PA12-60(f) decrease as pressure increases, reflecting faster molecular diffusion on the pore surface at low pressure until saturation is reached (Figure 9a). This behavior suggests that increasing ZIF-67 mass loading aligns with the hydrogen diffusion pattern, indicating good dispersion and minimal pore blockage, even at higher mass loadings of ZIF-67.

$$b \times \left(1 - \exp\left(-\frac{x}{k}\right)\right) \qquad (2)$$

Equation (2) shows the LDF equation, where (*b*) and (*k*) are fitting parameters.
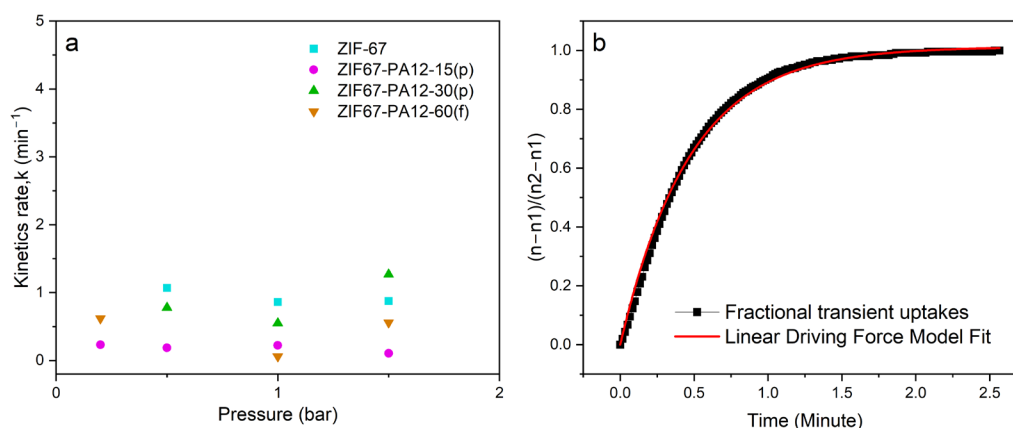
Figure 9. Hydrogen adsorption (**a**) kinetic rate, k, as a function of pressure at 77 K on ZIF-67, ZIF-67-PA12 distinct powder, and film samples. (**b**) The fitting result for ZIF-67 fractional transient uptake as a function of time at 77 k and 500 mbar in one pressure dosing step. n2 − n1 is the total uptake from time 1 to time 2 in one dosing step/isotherm. n − n1 represents the transient uptake.

4. Conclusions

This comprehensive investigation into ZIF-67-PA12 composites has clearly demonstrated the successful synthesis of both composite powders through in situ methods and films via ex situ techniques. The ex situ techniques applied to the film composites further illustrated the versatility and effectiveness of ZIF-67 integration, offering simpler processing for promising higher MOF content and reduced preparation in the manufacturing steps. Among the powder and film composites, ZIF-67-PA12-60(f) displayed a hydrogen capacity of 0.56 wt.%, whereas ZIF-67-PA12-30(p) reached 1.53 wt.%, building upon PA12's baseline capacity of 0.38 wt.%. This method notably optimized the surface characteristics and distribution of ZIF-67, enhancing the material's performance.

Recognizing the challenges in preserving in situ-prepared base MOF–polymer composite powders, which is a potential waste material in the PBF printing process, the research progressed to explore distinct mass loadings of ZIF-67 growth on printed PA12 films using ex situ synthesis. Compared to the in situ synthesis of ZIF-67-PA12 composites, the integration of ex situ synthesis in the fabrication of ZIF-67-PA12 membranes not only avoids the challenges associated with spreadability and processability in directly printing prepared ZIF-67-PA12 powder, but also significantly reduces waste in the printing process. This approach provides a viable pathway for large-scale manufacturing at a lower cost, thereby offering a practical and economical solution for hydrogen storage in mobile applications.

In practical applications, ensuring consistent material synthesis and managing costs are primary concerns in scaling up production. Cost in raw materials and energy consumption need to be managed, and a reliable, easy manufacturing routine needs to be demonstrated. Future research could explore combining PBF's capability for printing polymers into complex structures with other hydrogen storage materials, such as Mg-based and carbon-based materials, which can achieve a high hydrogen storage capacity exceeding 6 wt.% [9,11]. Integrating ex situ processes and 3D printing to fabricate MOFs or other materials with polymers would enable the creation of highly tailored geometries for specific storage needs, offering advantages in scalability and integration into complex systems.

Supplementary Materials: The following supporting information can be downloaded at: www.mdpi.com/xxx/s1. Table S1. Experimental data for different weight percentages of in situ ZIF-67-PA12 samples; Table S2. Experimental data for different weight percentages of ex situ ZIF-67-PA12 samples; Figure S1. Cross-sectional micrograph of printed PA12 film; Figure S2 (a-h). Elemental mapping of PA12 film and ZIF-67 dispersion on ZIF-67-PA12 film composites for mass loading (2, 10, 15, 20, 30, and 60).

References

1. Barthelemy, H.; Weber, M.; Barbier, F. Hydrogen storage: Recent improvements and industrial perspectives. *Int. J. Hydrog. Energy* **2017**, *42*, 7254–7262. https://doi.org/10.1016/j.ijhydene.2016.03.178.
2. Rivard, E.; Trudeau, M.; Zaghib, K. Hydrogen storage for mobility: A review. *Materials* **2019**, *12*, 1973.
3. Graetz, J. New approaches to hydrogen storage. *Chem. Soc. Rev.* **2009**, *38*, 73–82.
4. Rochat, S.; Tian, M.; Atri, R.; Mays, T.J.; Burrows, A.D. Enhancement of gas storage and separation properties of microporous polymers by simple chemical modifications. *Multifunct. Mater.* **2021**, *4*, 025002. https://doi.org/10.1088/2399-7532/ac005f.
5. Tian, M.; Rochat, S.; Fawcett, H.; Burrows, A.D.; Bowen, C.R.; Mays, T.J. Chemical modification of the polymer of intrinsic microporosity PIM-1 for enhanced hydrogen storage. *Adsorption* **2020**, *26*, 1083–1091. https://doi.org/10.1007/s10450-020-00239-y.
6. Abdalla, A.M.; Hossain, S.; Nisfindy, O.B.; Azad, A.T.; Dawood, M.; Azad, A.K. Hydrogen production, storage, transportation and key challenges with applications: A review. *Energy Convers. Manag.* **2018**, *165*, 602–627. https://doi.org/10.1016/j.enconman.2018.03.088.
7. Yang, H.; Ding, Z.; Li, Y.-T.; Li, S.-Y.; Wu, P.-K.; Hou, Q.-H.; Zheng, Y.; Gao, B.; Huo, K.-F.; Du, W.-J.; et al. Recent advances in kinetic and thermodynamic regulation of magnesium hydride for hydrogen storage. *Rare Met.* **2023**, *42*, 2906–2927. https://doi.org/10.1007/s12598-023-02306-z.
8. Ding, Z.; Li, H.; Shaw, L. New insights into the solid-state hydrogen storage of nanostructured LiBH4-MgH2 system. *Chem. Eng. J.* **2020**, *385*, 123856. https://doi.org/10.1016/j.cej.2019.123856.
9. Ding, Z.; Li, Y.; Yang, H.; Lu, Y.; Tan, J.; Li, J.; Li, Q.; Chen, Y.a.; Shaw, L.L.; Pan, F. Tailoring MgH2 for hydrogen storage through nanoengineering and catalysis. *J. Magnes. Alloys* **2022**, *10*, 2946–2967. https://doi.org/10.1016/j.jma.2022.09.028.
10. Ding, Z.; Lu, Y.; Li, L.; Shaw, L. High reversible capacity hydrogen storage through Nano-LiBH4 + Nano-MgH2 system. *Energy Storage Mater.* **2019**, *20*, 24–35. https://doi.org/10.1016/j.ensm.2019.04.025.
11. Ströbel, R.; Garche, J.; Moseley, P.T.; Jörissen, L.; Wolf, G. Hydrogen storage by carbon materials. *J. Power Sources* **2006**, *159*, 781–801. https://doi.org/10.1016/j.jpowsour.2006.03.047.
12. Ren, L.; Zhu, W.; Zhang, Q.; Lu, C.; Sun, F.; Lin, X.; Zou, J. MgH2 confinement in MOF-derived N-doped porous carbon nanofibers for enhanced hydrogen storage. *Chem. Eng. J.* **2022**, *434*, 134701. https://doi.org/10.1016/j.cej.2022.134701.
13. Almasoudi, A.; Mokaya, R. Preparation and hydrogen storage capacity of templated and activated carbons nanocast from commercially available zeolitic imidazolate framework. *J. Mater. Chem.* **2012**, *22*, 146–152. https://doi.org/10.1039/c1jm13314d.
14. Bazer-Bachi, D.; Assié, L.; Lecocq, V.; Harbuzaru, B.; Falk, V. Towards industrial use of metal-organic framework: Impact of shaping on the MOF properties. *Powder Technol.* **2014**, *255*, 52–59. https://doi.org/10.1016/j.powtec.2013.09.013.
15. Mallakpour, S.; Azadi, E.; Hussain, C.M. MOF/COF-based materials using 3D printing technology: Applications in water treatment, gas removal, biomedical, and electronic industries. *New J. Chem.* **2021**, *45*, 13247–13257. https://doi.org/10.1039/d1nj02152d.
16. Yang, S.J.; Kim, T.; Im, J.H.; Kim, Y.S.; Lee, K.; Jung, H.; Park, C.R. MOF-Derived Hierarchically Porous Carbon with Exceptional Porosity and Hydrogen Storage Capacity. *Chem. Mater.* **2012**, *24*, 464–470. https://doi.org/10.1021/cm202554j.
17. Shekhah, O.; Liu, J.; Fischer, R.A.; Woll, C. MOF thin films: Existing and future applications. *Chem. Soc. Rev.* **2011**, *40*, 1081–1106. https://doi.org/10.1039/c0cs00147c.
18. Chen, B.; Davies, R.; Chang, H.; Xia, Y.; Zhu, Y.; Ghita, O. In-situ synthesis of Metal Organic Frameworks (MOFs)-PA12 powders and their laser sintering into hierarchical porous lattice structures. *Addit. Manuf.* **2021**, *38*, 101774. https://doi.org/10.1016/j.addma.2020.101774.
19. Kirchon, A.; Feng, L.; Drake, H.F.; Joseph, E.A.; Zhou, H.C. From fundamentals to applications: A toolbox for robust and multifunctional MOF materials. *Chem. Soc. Rev.* **2018**, *47*, 8611–8638. https://doi.org/10.1039/c8cs00688a.
20. Lawson, S.; Snarzyk, M.; Hanify, D.; Rownaghi, A.A.; Rezaei, F. Development of 3D-Printed Polymer-MOF Monoliths for CO2 Adsorption. *Ind. Eng. Chem. Res.* **2019**, *59*, 7151–7160. https://doi.org/10.1021/acs.iecr.9b05445.

21. Channell, M.N.; Sefa, M.; Fedchak, J.A.; Scherschligt, J.; Bible, M.; Natarajan, B.; Klimov, N.N.; Miller, A.E.; Ahmed, Z.; Hartings, M.R. Toward 3D Printed Hydrogen Storage Materials Made with ABS-MOF Composites. *Polym. Adv. Technol.* **2018**, *29*, 867–873. https://doi.org/10.1002/pat.4197.

22. Qian, J.; Sun, F.; Qin, L. Hydrothermal synthesis of zeolitic imidazolate framework-67 (ZIF-67) nanocrystals. *Mater. Lett.* **2012**, *82*, 220–223. https://doi.org/10.1016/j.matlet.2012.05.077.

23. Wang, M.; Liu, J.; Guo, C.; Gao, X.; Gong, C.; Wang, Y.; Liu, B.; Li, X.; Gurzadyan, G.G.; Sun, L. Metal–organic frameworks (ZIF-67) as efficient cocatalysts for photocatalytic reduction of CO_2: The role of the morphology effect. *J. Mater. Chem. A* **2018**, *6*, 4768–4775. https://doi.org/10.1039/c8ta00154e.

24. Yu, Q.; Doan, H.V.; Xia, Y.; Hu, X.; Zhu, Y.; Ting, V.P.; Taheri, M.; Tian, M. Sustainable fabrication of metal-organic frameworks for improved hydrogen storage. *Int. J. Hydrog. Energy* **2024**, *81*, 371–381. https://doi.org/10.1016/j.ijhydene.2024.07.248.

25. Denisov, G.L.; Primakov, P.V.; Korlyukov, A.A.; Novikov, V.V.; Nelyubina, Y.V. Solvothermal Synthesis of the Metal-Organic Framework MOF-5 in Autoclaves Prepared by 3D Printing. *Russ. J. Coord. Chem.* **2020**, *45*, 836–842. https://doi.org/10.1134/s1070328419120030.

26. Ren, J.; Musyoka, N.M.; Langmi, H.W.; Swartbooi, A.; North, B.C.; Mathe, M. A more efficient way to shape metal-organic framework (MOF) powder materials for hydrogen storage applications. *Int. J. Hydrog. Energy* **2015**, *40*, 4617–4622. https://doi.org/10.1016/j.ijhydene.2015.02.011.

27. Ding, M.; Cai, X.; Jiang, H.L. Improving MOF stability: Approaches and applications. *Chem. Sci.* **2019**, *10*, 10209–10230. https://doi.org/10.1039/c9sc03916c.

28. Suh, M.P.; Park, H.J.; Prasad, T.K.; Lim, D.W. Hydrogen storage in metal-organic frameworks. *Chem. Rev.* **2012**, *112*, 782–835. https://doi.org/10.1021/cr200274s.

29. Chen, L.; Zhang, X.; Cheng, X.; Xie, Z.; Kuang, Q.; Zheng, L. The function of metal-organic frameworks in the application of MOF-based composites. *Nanoscale Adv.* **2020**, *2*, 2628–2647. https://doi.org/10.1039/d0na00184h.

30. Neville, G.M.; Jagpal, R.; Paul-Taylor, J.; Tian, M.; Burrows, A.D.; Bowen, C.R.; Mays, T.J. Freeze casting of porous monolithic composites for hydrogen storage. *Mater. Adv.* **2022**, *3*, 8934–8946. https://doi.org/10.1039/d2ma00710j.

31. Panchariya, D.K.; Rai, R.K.; Anil Kumar, E.; Singh, S.K. Core-Shell Zeolitic Imidazolate Frameworks for Enhanced Hydrogen Storage. *ACS Omega* **2018**, *3*, 167–175. https://doi.org/10.1021/acsomega.7b01693.

32. Ntouros, V.; Kousis, I.; Pisello, A.L.; Assimakopoulos, M.N. Binding Materials for MOF Monolith Shaping Processes: A Review towards Real Life Application. *Energies* **2022**, *15*, 1489. https://doi.org/10.3390/en15041489.

33. Broom, D. The accuracy of hydrogen sorption measurements on potential storage materials. *Int. J. Hydrog. Energy* **2007**, *32*, 4871–4888. https://doi.org/10.1016/j.ijhydene.2007.07.056.

34. Wu, C.-D.; Lin, W. Heterogeneous asymmetric catalysis with homochiral metal-organic frameworks: Network-structure-dependent catalytic activity. *Angew. Chem. Int. Ed. Engl.* **2007**, *46*, 1075–1078. https://doi.org/10.1002/anie.200602099.

35. Wu, X.; Liu, W.; Wu, H.; Zong, X.; Yang, L.; Wu, Y.; Ren, Y.; Shi, C.; Wang, S.; Jiang, Z. Nanoporous ZIF-67 embedded polymers of intrinsic microporosity membranes with enhanced gas separation performance. *J. Membr. Sci.* **2018**, *548*, 309–318. https://doi.org/10.1016/j.memsci.2017.11.038.

36. Tian, M.; Rochat, S.; Polak-Kraśna, K.; Holyfield, L.T.; Burrows, A.D.; Bowen, C.R.; Mays, T.J. Nanoporous polymer-based composites for enhanced hydrogen storage. *Adsorption* **2019**, *25*, 889–901. https://doi.org/10.1007/s10450-019-00065-x.

37. Rubio-Martinez, M.; Avci-Camur, C.; Thornton, A.W.; Imaz, I.; Maspoch, D.; Hill, M.R. New synthetic routes towards MOF production at scale. *Chem. Soc. Rev.* **2017**, *46*, 3453–3480. https://doi.org/10.1039/c7cs00109f.

38. Ren, J.; Langmi, H.W.; North, B.C.; Mathe, M. Review on processing of metal-organic framework (MOF) materials towards system integration for hydrogen storage. *Int. J. Energy Res.* **2015**, *39*, 607–620. https://doi.org/10.1002/er.3255.

39. Li, R.; Yuan, S.; Zhang, W.; Zheng, H.; Zhu, W.; Li, B.; Zhou, M.; Wing-Keung Law, A.; Zhou, K. 3D Printing of Mixed Matrix Films Based on Metal-Organic Frameworks and Thermoplastic Polyamide 12 by Selective Laser Sintering for Water Applications. *ACS Appl. Mater. Interfaces* **2019**, *11*, 40564–40574. https://doi.org/10.1021/acsami.9b11840.

40. El-Mehalmey, W.A.; Safwat, Y.; Bassyouni, M.; Alkordi, M.H. Strong Interplay between Polymer Surface Charge and MOF Cage Chemistry in Mixed-Matrix Membrane for Water Treatment Applications. *ACS Appl. Mater. Interfaces* **2020**, *12*, 27625–27631. https://doi.org/10.1021/acsami.0c06399.

41. Cheng, Y.; Ying, Y.; Japip, S.; Jiang, S.-D.; Chung, T.-S.; Zhang, S.; Zhao, D. Advanced Porous Materials in Mixed Matrix Membranes. *Adv. Mater.* **2018**, *30*, e1802401. https://doi.org/10.1002/adma.201802401.

42. Egorov, V.; Gulzar, U.; Zhang, Y.; Breen, S.; O'Dwyer, C. Evolution of 3D Printing Methods and Materials for Electrochemical Energy Storage. *Adv. Mater.* **2020**, *32*, e2000556. https://doi.org/10.1002/adma.202000556.

43. Lahtinen, E.; Precker, R.L.M.; Lahtinen, M.; Hey-Hawkins, E.; Haukka, M. Selective Laser Sintering of Metal-Organic Frameworks: Production of Highly Porous Filters by 3D Printing onto a Polymeric Matrix. *Chempluschem* **2019**, *84*, 222–225. https://doi.org/10.1002/cplu.201900081.

44. Lieu, W.Y.; Fang, D.; Tay, K.J.; Li, X.L.; Chu, W.C.; Ang, Y.S.; Li, D.S.; Ang, L.K.; Wang, Y.; Yang, H.Y. Progress on 3D-Printed Metal-Organic Frameworks with Hierarchical Structures. *Adv. Mater. Technol.* **2022**, *7*, 2200023. https://doi.org/10.1002/admt.202200023.

45. Gao, Y.; Lalevée, J.; Simon-Masseron, A. An Overview on 3D Printing of Structured Porous Materials and Their Applications. *Adv. Mater. Technol.* **2023**, *8*, 2300377. https://doi.org/10.1002/admt.202300377.

46. Yang, L.; Wang, L.; Chen, Y. Solid-state shear milling method to prepare PA12/boron nitride thermal conductive composite powders and their selective laser sintering 3D-printing. *J. Appl. Polym. Sci.* **2019**, *137*, 48766. https://doi.org/10.1002/app.48766.

47. Afshari, M.; Bakhshi, S.; Samadi, M.R.; Afshari, H. Optimizing the mechanical properties of TiO$_2$/PA12 nano-composites fabricated by SLS 3D printing. *Polym. Eng. Sci.* **2022**, *63*, 267–280. https://doi.org/10.1002/pen.26203.

48. Tomanik, M.; Zmudzinska, M.; Wojtkow, M. Mechanical and Structural Evaluation of the PA12 Desktop Selective Laser Sintering Printed Parts Regarding Printing Strategy. *3D Print. Addit. Manuf.* **2021**, *8*, 271–279. https://doi.org/10.1089/3dp.2020.0111.

49. Perrot, V.; Roussey, A.; Benayad, A.; Veillerot, M.; Mariolle, D.; Sole-Daura, A.; Mellot-Draznieks, C.; Ricoul, F.; Canivet, J.; Quadrelli, E.A.; et al. ZIF-8 thin films by a vapor-phase process: Limits to growth. *Nanoscale* **2023**, *15*, 7115–7125. https://doi.org/10.1039/d3nr00404j.

50. El-Sharkawy, I.I. On the linear driving force approximation for adsorption cooling applications. *Int. J. Refrig.* **2011**, *34*, 667–673. https://doi.org/10.1016/j.ijrefrig.2010.12.006.